


Article

Graphite Content Identification with Laboratory and Field Spectral Induced Polarization Measurements

Tímea Katona ^{1,*}, Adrián Flores-Orozco ^{1,*} , Lukas Aigner ¹ and Christian Benold ²

¹ Research Unit Geophysics, Department of Geodesy and Geoinformation, TU Wien, Wiedner Hauptstrasse 8–10, 1040 Vienna, Austria; lukas.aigner@geo.tuwien.ac.at

² GeoSphere Austria, Geophysics Department, Neulinggasse 38, 1030 Vienna, Austria; christian.benold@geosphere.at

* Correspondence: timea.katona@tuwien.ac.at (T.K.); adrian.flores-orozco@geo.tuwien.ac.at (A.F.-O.)

Abstract: Graphite, a critical raw material, prompts interest in assessing former quarries for volumetric content, driving the need for accurate prospection techniques. We explore the efficacy of spectral induced polarization (SIP) imaging at field scale for this purpose. Field measurements in a quarry with unknown graphite content underscore the need for assessment before drilling due to abrupt topography. Due to the lack of ground truth required to calibrate existing petrophysical models, we propose using SIP laboratory measurements to achieve the quantitative interpretation of the imaging results. We conducted experiments at two scales: rock plugs for material response and ground rocks of varying sizes for textural analysis. The rock plugs allow us to investigate the response of the material, while the ground samples permit us to understand changes in the SIP response for varying textural properties. Our lab work establishes power-law relationships between polarization (expressed in terms of normalized chargeability) and graphite content, as well as relaxation time and grain size. Salinity dependence is noted between chargeability, normalized chargeability, and relaxation time. Utilizing these findings, we provide a quantitative interpretation of field SIP imaging results.

Keywords: graphite content; geophysical imaging methods; electrical conductivity; spectral induced polarization; Cole-Cole parameters

check for
updates

Citation: Katona, T.; Flores-Orozco, A.; Aigner, L.; Benold, C. Graphite Content Identification with Laboratory and Field Spectral Induced Polarization Measurements. *Appl. Sci.* **2024**, *14*, 3955. <https://doi.org/10.3390/app14103955>

Academic Editor: Jakub Ciazela

Received: 13 April 2024

Revised: 3 May 2024

Accepted: 5 May 2024

Published: 7 May 2024



Copyright: © 2024 by the authors. Licensee MDPI, Basel, Switzerland. This article is an open access article distributed under the terms and conditions of the Creative Commons Attribution (CC BY) license (<https://creativecommons.org/licenses/by/4.0/>).

1. Introduction

Graphite is an essential mineral used in batteries, brake linings, or lubricants and graphite tailing can be used as a cement to produce concrete. Additionally, graphite can be used to increase the frost resistance in building materials [1] and to decrease the electrical resistivity in concrete for deicing or snow melting. The importance of graphite demands the prospection of new ores and the evaluation of former quarries. Jara et al. provide insight into the current graphite market and its increasing trend [2], while Rui et al. offer insights into resource utilization, environmental aspects, and sustainability [3]. Geophysical methods are a suitable and relatively cost-efficient alternative for exploration as they do not require drilling or analysis of samples. The electrical and electromagnetic (EM) geophysical techniques aim at quantifying changes in the electrical properties of the subsurface; thus are well suited to characterize graphite deposits, considering that graphite is related to high electrical conductivity [4]. However, as described in a recent study by Aigner et al., in the case of graphite, EM data can be strongly affected by induced polarization (IP) effects, which dominate the electrical conductivity [5]. Electrical and electromagnetic measurements have revealed much lower conductivity and IP response for measurements conducted in other environments with organic carbon such as coal [6], peatlands [7], or municipal solid waste [8]. Thus, the induced polarization method is the most attractive technique for characterizing graphite ores. The so-called spectral-induced polarization (SIP) method has a long history of being used in metallic ore exploration [9,10]. In the

case of graphite, high electrical conductivity and polarization have been observed in laboratory measurements [11,12], with recent studies reporting changes in the frequency-dependence of the electrical properties for varying grain size, chemical parameters and anisotropy [13–15]. However, field investigations are still rare [16,17]. Different aspects limit the application at the field scale of the SIP method. On the one hand, measurements in electrical conductors (such as graphite) are related to low voltages; thus, low signal-to-noise ratio (S/N). On the other hand, electrical conductors enhance parasitic electromagnetic (EM) fields, commonly referred to as EM coupling, which are also a source of systematic errors in SIP readings [18,19]. EM inductive coupling linearly increases with subsurface conductivity and measurement frequency and contaminates the SIP surveys commonly above 10 Hz [20–23]. Flores Orozco et al. revealed that EM coupling can already affect SIP measurements at 1 Hz in conductive media due to cross-talking in multicore cables commonly used in geophysical prospecting [24].

In the presence of electrical conductors such as graphite, the electrical conduction is dominated by the current flowing across the conductive mineral (electronic conduction). The strong polarization response originates from the so-called electrode polarization [25], which accounts for the polarization of the free charges within conductors and for the electrical double layer (EDL) formed at the fluid-mineral interface [20,26–28]. It has been observed that the frequency-dependence of the polarization response is correlated to the size, volume, and texture of the metallic minerals [20,27,28]. Slater et al. showed a power-law relationship between the polarization magnitude and pore volume, comparable in non-metallic and metallic soils [29]. Revil et al. have presented a new mechanistic model considering intragrain polarization in conductive particles [26,30–33]. Such a model assumes that the Stern layer polarization dominates the main response and that the particle behaves dielectric once the polarization is fully established. Alternatively, Wong and Bucker et al. consider the electrical conductor as a leaking capacitor due to the interchange of ions between the mineral and fluid [25,27,28]. Thus, the polarization of charges within the conductive material never results in the form of a dielectric, but in an overall decrease in the amplitude of the polarization response and a shift of the polarization peak towards lower frequencies [25,27,28].

At the field scale, Börner et al. investigated the SIP response of graphitic black schists of a Himalayan shear zone (in Nepal) [17]. They observed a high polarization response (around 1 Hz parallel to the foliation) and concluded that the black schist is characterized by high anisotropy. Abdulsamad et al. proposed a linear model to estimate the volume fraction of graphite, applying the model proposed by Revil et al. and found that the conductivity of the background material controls the conductivity of the material, and the chargeability depends linearly on the volumetric graphite content [16,26,31]. Nonetheless, Wu and Peruzzo found that besides the volumetric concentration of the graphite, the fluid chemistry (pore fluid salinity and pH) also controls the polarization response [15].

In this study, we aim to evaluate the applicability of the SIP method to quantify the remaining graphite content in the mining tailings of a former graphite quarry. The graphite deposit has been reported from geological observations between two faults, as depicted in Figure 1a, and the graphite-rich formation is expected to continue under the subsurface towards the South-West direction. However, no drilling is available to justify such a hypothesis. Hence, we propose an alternative methodology for the application (i.e., calibration) of existing petrophysical models towards the quantitative interpretation of SIP imaging results. We compared SIP signatures obtained in the field and laboratory to develop a semi-empirical model linking the graphite content with the amplitude of the polarization effect. Here, laboratory measurements are conducted in rock plugs (to avoid changes in the geometry of the pore scale), followed by measurements in ground samples, where we evaluate the frequency dependence of IP readings by changing the texture of the material. Chemical analysis of the ground samples was conducted to obtain the graphite content. Hence, our objective is to interpret the SIP imaging results regarding graphite content and its textural properties.

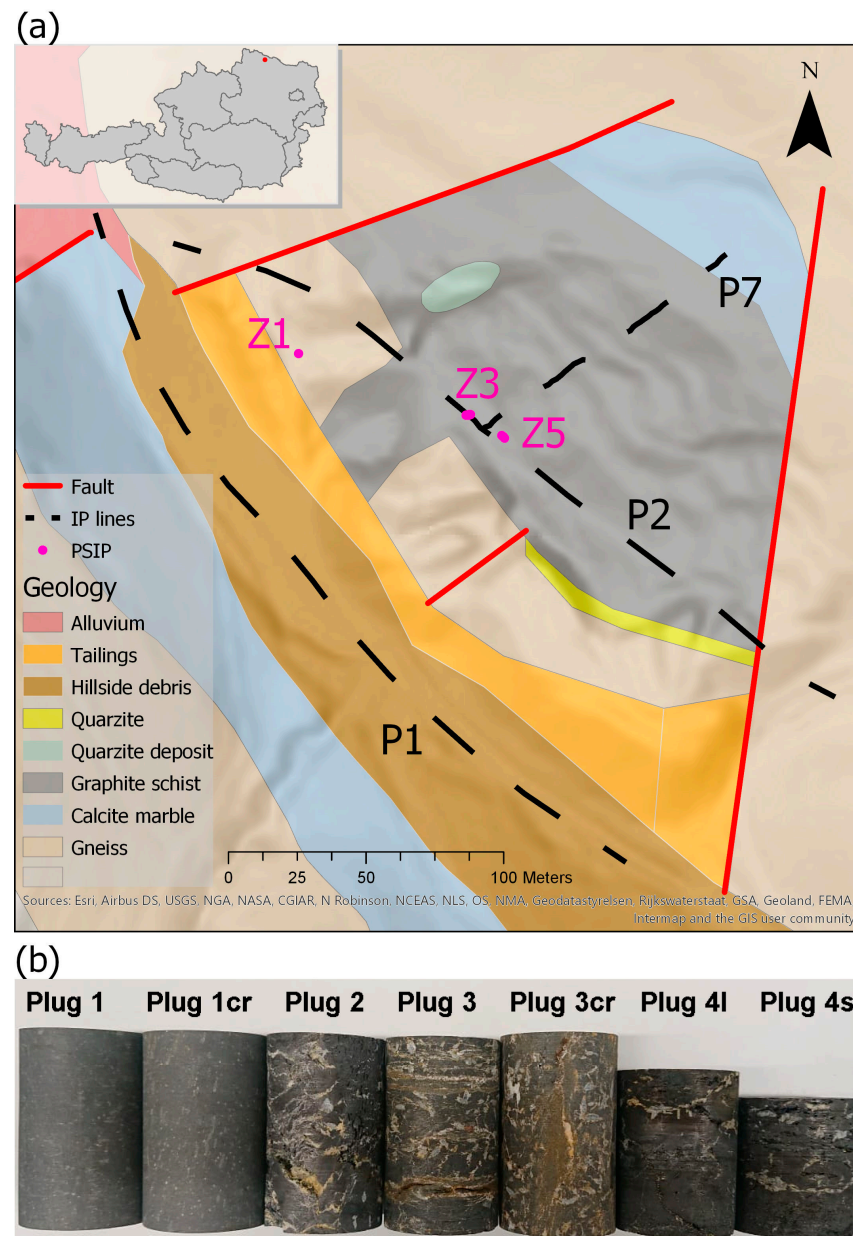


Figure 1. (a) Location and geological settings of the measured spectral induced polarization (SIP) lines and measurements conducted with the Portable SIP Unit (PSIP) near Zettlitz, Lower Austria. The GeoSphere Austria provided the geological information. (b) Core plugs, extracted from 4 different rocks collected at the site. The plug 4l (long) and 4s (short) were drilled from the same rock we have ground to receive the graphite sediments for further laboratory measurements and analysis. The cr denotes that the core was drilled perpendicular to the corresponding numbered paired core (e.g., 1 and 1cr).

2. Materials and Methods

2.1. Site Description

The study area is located close to Zettlitz in Lower Austria, where a graphite quarry was active between 1855 and 1966. The deposit comprises graphite schist, surrounded by gneiss and calcite, as presented in Figure 1a. The graphite is present as inclusions generally occurring in the immediate vicinity or directly between layers of marble and paragneiss. Graphite schists form lenses and bands centimeters to meters thick, while the graphite gneiss forms zones up to tens of meters thick within the paragneiss [34]. The graphite is either evenly distributed or enriched on the foliation surfaces. The structure of

the graphite bodies is tectonically heavily overprinted, so the graphite is mostly tectonically rolled out into lens-shaped bodies, which form very irregular deposit bodies. Locally, the graphite bodies can reach a significant thickness (a few centimeters) but often wedge out unexpectedly, making alignment of the deposit during mining quite difficult. In addition to the deposits used for mining in this area, many smaller, economically insignificant graphite lenses can be mapped very quickly, even in unexplored areas, due to the characteristic blackish soil color [35].

2.2. The Spectral Induced Polarization Method

The induced polarization (IP) imaging method, also known as complex resistivity (or by its inverse the complex conductivity, CC) imaging, or electrical impedance tomography, is an extension of the electrical resistivity tomography (ERT) method. It is based on four-electrode measurements, where two electrodes are used to inject current (current dipole), and another pair of electrodes is used to measure the resulting voltage (potential dipole). Modern devices can simultaneously measure tens of potential dipoles for a given current dipole, permitting data collection with high spatial resolution and reduced acquisition times [36]. IP data can be collected in the time domain (TDIP) or the frequency domain (FD). Most commercial instruments work in TDIP, using direct current, with measurements of the transfer resistance during the current injection. At the same time, the integral chargeability is computed from voltage measurements collected after shutting off the current to record the decay of the secondary voltage [22]. In FDIP, an alternating current is injected into the ground to measure the resulting electrical impedance in terms of its magnitude (i.e., transfer resistances) and the phase shift between the periodic voltage and current signals. FDIP measurements can be conducted at different frequencies using the so-called spectral IP (SIP) method to gain information about the frequency dependence of the electrical properties. Recent studies have proposed using TDIP measurements to record the full waveform to gain information about the frequency dependence [37,38]. Nevertheless, we will only investigate SIP signatures collected from FDIP in this study. Further details of the IP method can be found in the books by Binley and Slater or Sumner, as well as the studies by Ward and Binley and Kemna [22,39–41].

IP imaging measurements (TDIP or FDIP) can be inverted to solve the spatial (i.e., lateral and vertical) changes of the complex resistivity in the subsurface. The complex conductivity (σ^*)—or its inverse, the complex resistivity (ρ , with $\sigma^* = 1/\rho$)—can be expressed in terms of its real (or in-phase, σ') and imaginary (or quadrature, σ'') components, or by its magnitude ($|\sigma|$) and phase (φ), such as

$$\sigma^* = \sigma' + i\sigma'' = |\sigma|e^{i\varphi} \quad (1)$$

where $i = \sqrt{-1}$. The real part of the complex conductivity (σ') is related to the ohmic conduction, while the imaginary part (σ''), is related to the polarization.

We use the Cole-Cole type model as proposed by Pelton et al. to describe the frequency dependence of the complex resistivity in SIP measurements. The Pelton model (PM) can be expressed in terms of the electrical resistivity by [20]:

$$\rho^* = \rho_0 \left[1 - M \left(1 - \frac{1}{1 + (i\omega\tau)^c} \right) \right] \quad (2)$$

where M is the chargeability (describing the amplitude of the polarization), ρ_0 the low-frequency limit of the resistivity, c is the dispersion coefficient and $\tau = \frac{1}{2\pi f_c} \frac{1}{(1-M)^{\frac{1}{c}}}$ is the relaxation time, with f_c being the characteristic frequency at which the maximum of the imaginary part of the complex resistivity is observed. The ratio of the chargeability and the ρ_0 gives the normalized chargeability:

$$M_n = \frac{M}{\rho_0} \quad (3)$$

We obtained the fit of the PM to our measured spectra (field and laboratory data) using routines developed by Maximilian Weigand, which are part of the Python geophysical imaging and modeling library pyGIMLi [42].

2.3. SIP Data Collection at the Field Scale

We collected SIP data along seven lines using different measurement setups from which we present three representative lines (P1, P2 and P7 in Table 1). Line P1 has an orientation NE-SW, and it is located outside the graphite quarry along a forest road (see Figure 1a), where the graphite is not observed at the surface but is expected to be located in the subsurface. Lines P2 (with an orientation NE-SW also) and P7 (perpendicular to P2) are located at the quarry where graphite content is observed at the surface (see Figure 1a) but its extension at depth is unknown. The topographical features of the quarry and the dense vegetation of the study site influenced the orientation of the IP lines. Profile P1 and P7 measurements were collected with 64 electrodes and a spacing of 5 m and 2 m between them, respectively, whereas measurements in P2 were collected with 32 electrodes with a separation of 10 m between them. To increase the resolution of our investigation, a second measurement, which we refer to as P2b, was conducted at P2 with 64 electrodes and 2 m electrode separation (with both profiles P2 and P2b centered on the same point). All electrodes are made of stainless steel and have a diameter of 10 mm. We used the DAS-1 (from Multi-Phase Technologies, LLC) to collect FDIP data. SIP measurements were collected in the frequency range between 0.1 Hz and 225 Hz in all profiles. However, data collected above 25 Hz revealed noisy pseudosections and were excluded from the analysis. We used a dipole-dipole configuration [43] using the eight measuring channels available in the DAS-1. Thus, voltage measurements are collected in eight adjacent potential dipoles for each current dipole, always ahead of the current dipole to avoid contamination of the data caused by remnant polarization of the electrodes. For the 10 m and 2 m electrode separation profiles, we used coaxial cables to connect the electrodes and the measuring device to minimize distortion of the data associated with cross-talking between the cables [18,19,44], with the shield of the coaxial cable running together into a ground electrode (as presented in Flores Orozco et al. [24]).

Table 1. Measurement setup in terms of the name of the profile (ID), frequency range of the spectral induced polarization (SIP) measurements, profile length and electrode spacing in meters, and electrode configuration (DD—dipole-dipole).

ID	SIP (Hz)	Profile Length	Electrode Spacing	Configuration	Direction
P1	1–225	315 m	5 m	DD	NW-SE
P2	0.1–225	310 m	10 m	DD	NW-SE
P2b	0.1–225	126 m	2 m	DD	NW-SE
P7	0.1–225	124 m	2 m	DD	NE-SW
Z1, Z3, Z5	0.1–10,000	1.5 m	0.5 m	Wenner	-

To obtain a broader frequency spectrum and enhance the spectral resolution, in-situ IP spectra were collected with a 4-electrode array at three selected points, referred to as Z1, Z3 and Z5 (Figure 1a), using the PSIP unit (from Ontash & Ermac, NJ, USA). This electrical impedance spectrometer is commonly used for laboratory investigations [39]. Those in-situ spectra were collected with a single quadrupole using stainless steel electrodes with a separation of 50 cm in a Wenner configuration. We collected data at 58 frequencies between 0.1 Hz and 20,000 Hz, with a distribution of eleven measurements per decade.

In the case of the imaging dataset, we filtered the raw data independently for each frequency (0.1–25 Hz) by removing readings that diverge significantly from the expected smooth change in the pseudosections. After the first filtering, we removed quadrupoles not found in all frequencies, as required to resolve for inversion results with relatively the same frequency in the 0.1 Hz and 25 Hz range. For the inversion of the filtered datasets, we used the smoothness-constrained least-squares algorithm CRTomo by Kemna [45], which allows

the data to be fitted to a level of confidence specified by an error model. The error model was empirically defined from different inversion results to obtain an error-weighted RMS equal to 1. The inversion was done independently for data sets collected at each frequency.

2.4. SIP Measurements and Chemical Analysis of Samples in the Laboratory

Laboratory measurements allow us to investigate the frequency dependence of the graphite-rich rocks, minimizing electromagnetic sources of noise, which cannot be avoided in field SIP imaging data. Rock samples were taken for laboratory measurements from the site near the PSIP measurements and the DAS-1 line P2b (see Figure 1). After the SIP measurements, X-ray fluorescence spectroscopy and LECO analysis were conducted on four rock samples to obtain the chemical composition (see Table 2). The Epsilon 5 X-ray fluorescence analyzer from analytical measured the elemental contents. The method measures the concentration of main oxide elements in %. The silicon content varies within the samples between 35.0% and 37.0%, and the concentration of aluminum oxide between 8.9% and 11.5%. Sample Size d4 contains higher readings of FeO (2.1%) and S (1.1%), indicating a higher pyrite content possibility. The other measured parameters show slight variations. The carbon content of the samples varies between 44.2% and 47.7%. These concentrations were determined using the carbon measurement of the LECO C/S 200 (Inductive combustion of the sample and measurement of the CO₂ concentration within an IR measuring cell).

Table 2. Laboratory analysis (X-ray fluorescence spectroscopy and LECO analysis) of four graphite sediments collected at the site. The grain sizes of the analyzed samples (*d*) are given for comparison.

Elements	<i>d</i> = 1–2 mm (%)	<i>d</i> > 10 mm (%)	<i>d</i> < 0.45 mm and <i>d</i> = 0.45–1 mm (%)	<i>d</i> = 0.45–1 mm and <i>d</i> > 10 mm (%)
SiO ₂	35.0	37.0	36.0	36.0
TiO ₂	0.6	0.5	0.6	0.5
Al ₂ O ₃	9.4	8.9	11.5	9.9
FeO	1.0	2.1	0.9	1.5
MnO	0.01	<0.01	0.01	0.01
MgO	<1	<1	<1	<1
CaO	<1	<1	<1	<1
Na ₂ O	0.9	0.7	0.9	1.0
K ₂ O	3.8	4.2	3.7	4.1
P ₂ O ₅	<0.5	<0.5	<0.5	<0.5
S	0.5	1.1	0.6	0.8
H ₂ O ^{110 °C}	0.3	0.3	0.3	0.2
H ₂ O+	<0.1	<0.1	<0.1	<0.1
C	47.7	44.2	45.1	45.4
Summe	99.2	99.0	99.5	99.3

SIP laboratory measurements were conducted on two scales: rock plugs and ground material. For all laboratory measurements, the PSIP instrument was used to collect 61 frequencies in the range between 0.01 and 10,000 Hz using ten measurements per decade.

SIP measurements in rock plugs were used to investigate the intrinsic SIP response of the rocks (i.e., without grinding). To this end, we extracted seven core plugs from the rock samples mentioned above, with the plugs drilled in different directions to investigate possible anisotropy (Figure 1b). Plugs 1, 1cr, 3 and 3cr were drilled from the same rocks (cr denotes a plug extracted at the same position but perpendicularly), while for a fourth sample, plugs were extracted only in one direction but with different lengths (4l and 4s). The core plugs have a radius of 19 mm and lengths between 40 and 62 mm (Table 3). SIP measurements in the rock plugs were conducted in a sample holder similar to the one used by Bairlein et al. [46], with a length of 250 mm and a radius of 19.5 mm. Non-polarizing voltage electrodes are located in the middle of the sample holder at a distance of 50 mm

from the plate electrodes used for the current injection, which are made of stainless steel found at both ends of the column.

Table 3. Cole-Cole parameter of the core plugs in terms of chargeability (M), normalized chargeability (M_n) and relaxation time, the length and volume of the plugs, and the percentage of volume covered by a plug within the measurement cell.

id	M	M_n	τ (s)	L (cm)	V (cm ³)	V_c (%)
plug1	0.96	0.0063	12.47	6.00	68.05	22.79
plug1cr	0.99	0.0380	14.80	6.00	68.05	22.79
plug2	0.96	0.0642	8.75	6.00	68.05	22.79
plug3	0.91	0.0262	94.08	6.00	68.05	22.79
plug3cr	0.96	0.0317	19.17	6.20	70.32	23.55
plug4s	0.50	0.0036	5.56	4.00	45.36	15.19
plug4l	0.55	0.0105	7.04	5.00	56.71	18.99

To investigate the SIP response for varying textural properties, we ground the same rock that was used to extract the plugs 4s and 4l. Grinding was conducted to different degrees to obtain samples with four different grain sizes (d): fine ($d < 0.45$ mm) denoted as d1, medium (d between 0.45 and 1 mm) denoted as d2, coarse (between 1 and 2 mm) denoted as d3, and large (>10 mm) denoted as d4. SIP measurements in these samples were conducted in a column with a length of 300 mm and a radius of 25 mm. Two plate electrodes are located at each end of the column and are used to inject current, while two non-polarizing Ag/AgCl electrodes (based on Inamdar et al. [47]) are located equidistant in the column (100 mm separation) to collect the electrical voltage. The columns were filled with ground graphite particles disseminated in quartz sand and fully saturated with demineralized water. Besides the rock samples, we conducted SIP measurements on commercial graphite powder with a maximum grain size of 0.075 mm provided by Carl Roth GmbH. Such commercial samples were built with a graphite volume content of 2% disseminated in silica sand. The commercial samples were fully saturated, and measurements were collected at different steps after increasing the pore fluid salinity (in the range between 0.005 and 0.25 S/m) by adding Sodium-chloride (NaCl) to demineralized water. The idea was to have a well-controlled grain size and evaluate changes in the SIP response by varying fluid conductivity to improve the interpretation of our field signatures.

3. Results and Discussion

3.1. The Identification of Graphite-Rich Areas from Field IP Imaging Results at 1 Hz

Figure 2 presents the complex conductivity imaging results for P1 (Figure 2a–d) and P7 (Figure 2e–h) in terms of in-phase and quadrature conductivity. The two profiles show different features, as measurements in P1 were conducted in the area with less graphite content, and P7 is located in the middle of the graphite quarry. Along P1, both in-phase and quadrature conductivity show the highest values in the first 100 m along profile direction; whereas for P7 the highest values are observed within the first 70 m along profile distance. Figure 2 reveals that the anomalies associated with high conductivity (σ') and polarization (σ'') values are one order of magnitude higher at P7 than at P1, with maximum values of $\sigma' > 200$ mS/m, $\sigma'' > 20$ mS/m in P7, and $\sigma' > 30$ mS/m, $\sigma'' > 3$ mS/m in P1. The increase in both conductivity and polarization values observed in P7 is in agreement with the geological setting, as we expect a higher graphite content in this area than in P1.

Figure 2 reveals shallow inversion results with highly conductive anomalies, whereas deeper model parameters can be resolved in less conductive areas, due to the low signal-to-noise ratio (S/N) observed in highly conductive graphite rocks. Measurements in those areas are related to low voltage readings, i.e., low transfer resistances or impedance magnitudes. Such low voltage readings (<1 mV) are more susceptible to distortions due to noise associated with the galvanic contact (between electrodes and ground) and changes in the surface cover, thus resulting in low signal-to-noise ratios (S/N) observed in measurements

in Zettlitz. We also note that even if the graphite provides a target with high polarization, the signal strength is dominated by the electrical impedance amplitude, i.e., the voltage-to-current ratio. Thus, high current densities injected and low voltage measurements lead to light distortions in the data due to low values in the impedance amplitude, even if the impedance phase readings are high. Besides the high conductivity of the subsurface, increasing the separation between current and potential dipoles also decreases the voltage measurements and the S/N; thus limiting the ability of surface measurements to reach deep areas. Accordingly, we observe in Figure 2 that only shallow model parameters are resolved along the first 80 m along P7 (maximum depth of investigation of ca. 2 m) at the highly conductive (>100 mS/m) zone, whereas deeper model parameters are resolved in less conductive zones between 80 m and 130 m distance. The filtering of readings with poor S/N results in the removal of a larger number of “deep” readings within the first half of P7, associated to large separations between the current and potential dipoles, This is observed in the imaging results with poor sensitivity below ca. 2 m depth. Accordingly, we cannot solve the highly conductive area related to the graphitic schist below the NE part of P7.

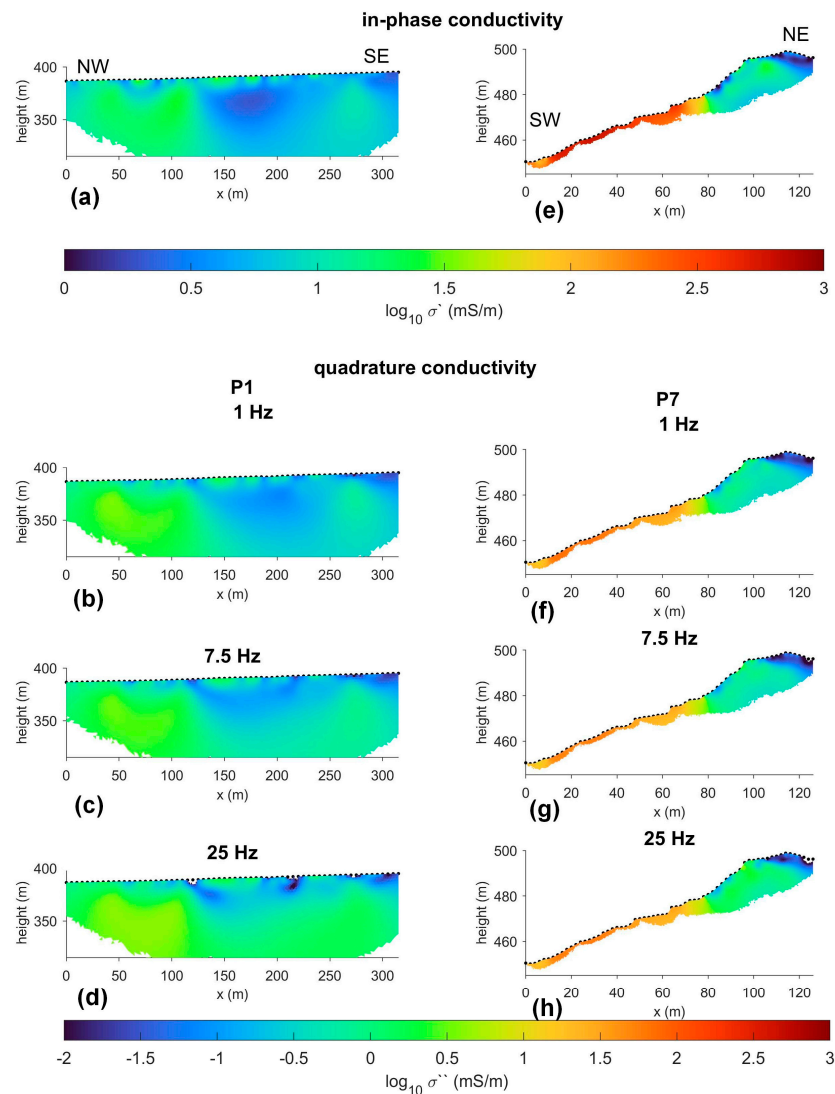


Figure 2. Complex conductivity imaging results collected along profiles (a–d) P1 and (e–h) P7, expressed as (a,e) in-phase conductivity and (b–d,f–h) quadrature conductivity. The position of the electrodes is marked with solid black dots at the surface.

Figure 3 presents the complex conductivity imaging results for the long profile P2 (Figure 3a–d) and the short profile P2b (Figure 3e–h). While P2 permits a deep investigation

and addresses lateral changes across a 330 m long profile, the profile P2b focuses on the anomaly characterized by high conductivity and polarization, as indicated in Figure 3. P2 shows a stronger frequency dependence than P2b, likely due to the contrasts between high and low σ' and σ'' values associated with the anomaly and areas outside it. Nevertheless, the imaging results obtained for P2 and P2b show similar features and high conductivity values, although the values in P2 are smaller than in P2b. The anomaly resolved between 80 m and 180 m along P2 is characterized by the highest σ^* values ($\sigma' > 200$ mS/m, $\sigma'' > 20$ mS/m) and corresponds to the materials with high graphite content. The small electrode spacing in P2b permits a better definition of the lateral extent of the graphite-rich area compared to the imaging results obtained for P2 (with larger electrode spacing). However, reducing the electrode spacing also reduces the S/N ratio in deep readings, and we cannot conclusively define the thickness of the graphite-rich zone with measurements in P2b, while the vertical contact can be resolved in P2 with a maximum thickness of ca. 20 m for the graphite-rich area.

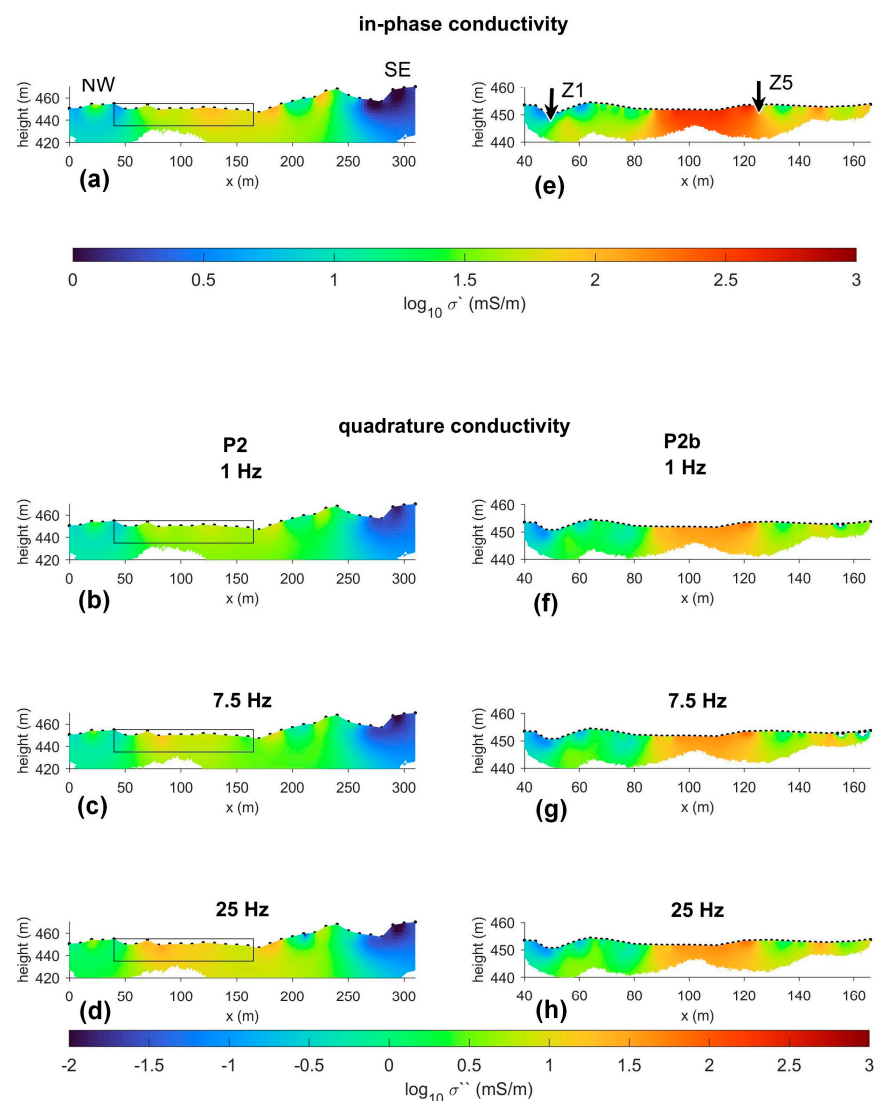


Figure 3. Complex conductivity imaging results collected along the long profile P2 with an electrode separation of (a–d) 10 m and (e–h) along the short profile P2b with an electrode separation of 2 m, expressed in terms of (a,e) in-phase conductivity and (b–d,f–h) quadrature conductivity. The position of the electrodes is marked with solid black dots at the surface. The black rectangle represents the position of P2b. The arrows on panel (e) represent the location of the 4 point in-situ measurements conducted with the PSIP device.

3.2. The Frequency-Dependence in SIP Measurements Conducted In-Situ and in the Lab

Figure 4 shows the complex conductivity spectra measured in the field and rock samples measured with the PSIP unit. The in-situ measurements reveal differences in the σ^* values measured between the graphite-rich area (indicated by the readings Z3 and Z5 in Figure 4a,b) and the area dominated by gneiss (indicated by the reading Z1 in Figure 4a,b). Although the values are different, the spectra are relatively similar. The difference in the values measured between the gneiss (Z1) and the graphite-rich area is practically two orders of magnitude (for both the conductivity and the polarization) and it is due to the high conductivity and polarization in good electrical conductors [25,27,28]. The measurements reveal a slight increase in the polarization values with increasing frequency. However, the lack of a dominant peak in the spectral response indicates well sorted materials, with no dominant grain size [20,23,27–30,48]. Moreover, the similar spectra resolved in the three locations indicate that, close to the surface, the materials are similarly well-sorted, independent of the graphite content.

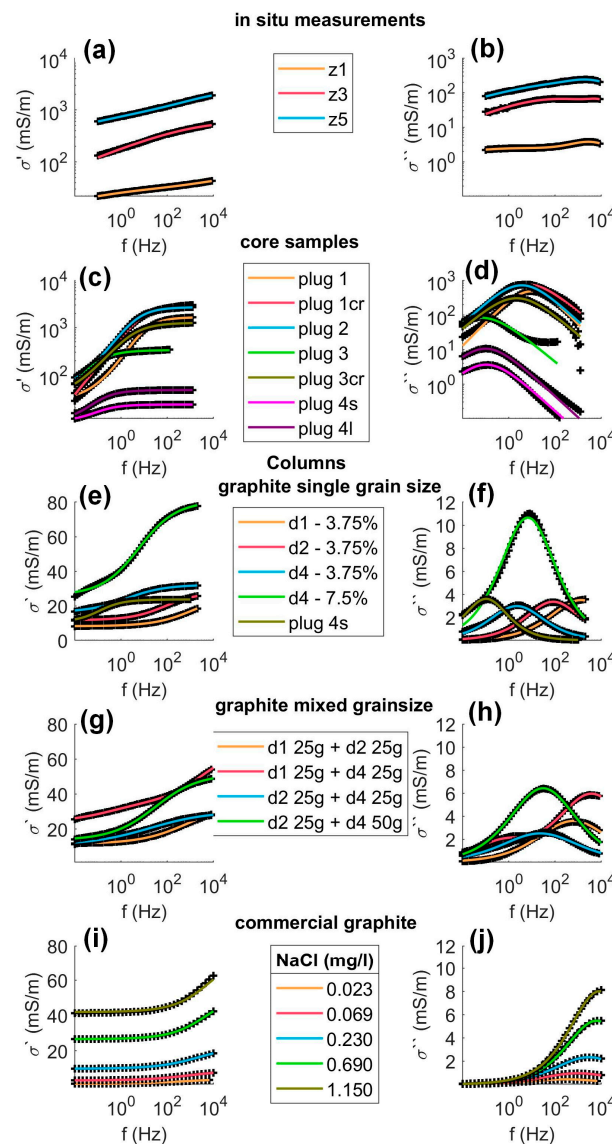


Figure 4. Measurements conducted (a,b) with the PSIP at the site, (c,d) laboratory complex conductivity spectra of the drilled core samples, (e–h) sediments collected at the quarry and (i–j) commercial graphite sediments in terms of (a,c,e,g,i) in-phase conductivity and (b,d,f,h,j) quadrature conductivity. The solid lines represent the Cole-Cole fit of the data. For visibility, the panels (e–j) range differs from the panels (a–d).

Laboratory measurements minimize the sources of data error and are not affected by modeling and inversion uncertainties affecting imaging field data. Hence, they allow us to understand the intrinsic properties of the material and support our interpretation. Figure 4c,d presents the spectra of the plugs, which represent the undisturbed samples. All spectra in the plugs reveal a clear frequency dependence, with a peak in the quadrature conductivity spectra at the low frequencies (<10 Hz). Although the spectra are similar, the polarization values differ for all spectra, with maximum values (i.e., at the critical frequencies) varying in the range between 1 mS/m and 1000 mS/m (Figure 4c,d). While plugs 1 and 2 reveal the highest polarization values (>500 mS/m), plug 4 reveals the lowest. The changes of the polarization response are related to the content of the electrical conductor, independent on the size of the sample, considering that plug 2 is larger than plug 4 (see Table 3). The spectra in Figure 4c,d reveal the significant heterogeneity in the polarization response of the study area. Moreover, it shows that in-situ spectra may provide only a limited insight into the subsurface properties, as they are limited in the depth and volume of investigation. In-situ spectra with large electrode spacing resulted only in noisy readings, as described for the imaging data sets, due to low voltages and high EM coupling in the data.

We extracted plugs with perpendicular directions (plug 1, 1cr, 3, and 3cr) from the same rocks to investigate anisotropy. Figure 4c,d shows that plugs 1 and 1cr do not exhibit significant anisotropy, as the measurements reveal consistent values and spectra. However, measurements of plugs 3 and 3cr demonstrate high differences in the critical frequency and its associated polarization values (100 mS/m and 300 mS/m for plugs 3 and 3cr, respectively), indicating that anisotropic effects in the electrical properties can not be neglected in the materials in the area where the rock was taken.

Figure 4 shows similar spectra for the measurements in plugs 1, 1cr, 2 and 3cr; thus suggesting consistent textural properties for the samples, which is not the case for the plugs 3, 4l and 4s. Direct measurements of pore-space geometry are possible [49]; however, it is associated with extra costs and efforts, especially when investigating a large number of samples. Hence, we propose a different approach to understanding the textural properties of the materials in our study area. We decided to destroy some rocks that were used to extract the plugs 4l and 4s to create samples with a controlled grain size. Ground samples then allow us to investigate the frequency dependence of the SIP measurements by changing the grain size of the ground samples. The spectra of the measurements in the ground samples with a well-defined grain size are presented in Figure 4e,f, while Figure 4g,h presents the spectra measured by the mixtures of samples with different grain sizes. In Figure 4e,f, we also include the spectra measured in plug 4s, which were drilled from the same rock where the grains were extracted. Although the weight of the plug 4s is 102 g, we observe similar polarization values (σ'') for the measurements in the plug and those in the samples with grain sizes d1, d2 and d4, associated with a 3.75% volumetric content of the sample corresponding to 50 g. In contrast, the σ'' values are three times lower (in the range of 3–4 mS/m) than those observed for measurements with the biggest grain size, d4 ($\sigma'' \sim 12$ mS/m), which are associated with larger sample volumetric content (7.5% corresponding to 100 g). Regarding the frequency-dependence, plots in Figure 4e–j show a shift in the quadrature conductivity peak to higher frequencies with decreasing grain size, as observed in other measurements performed in electronic semiconductors [20,29,50]. Moreover, the amplitude of the quadrature conductivity increases with the increasing graphite content, in agreement with mechanistic models [25–28,31]. Accordingly, we also observe increased characteristic relaxation time with increasing graphite grain size (Table 4) from the fitted Cole-Cole model for the different measurements.

Table 4. Cole-Cole parameter of the collected sediments in terms of chargeability (M), normalized chargeability (Mn) and relaxation time (τ), the volumetric graphite content (\varnothing) in the sand-graphite mixture and the mean grain diameter (d) of the graphite sediments.

Grain ID	M	M _n (mS/m)	τ (s)	\varnothing (%)	d (mm)
d1	0.35	0.0093	1.3×10^{-4}	1.88	0.45
d1	0.47	0.0094	1.61×10^{-4}	1.88	0.45
d1	0.71	0.0196	8.15×10^{-5}	3.76	0.45
d1	0.71	0.0204	8.39×10^{-5}	3.76	0.45
d1	0.85	0.0368	2.97×10^{-5}	5.63	0.45
d1	0.85	0.0329	3.87×10^{-5}	5.63	0.45
d1	0.88	0.1587	1.30×10^{-5}	7.51	0.45
d1	0.86	0.2773	6.66×10^{-6}	7.51	0.45
d1	0.88	0.9125	2.24×10^{-6}	15.02	0.45
d1	0.96	2.5545	7.09×10^{-8}	15.02	0.45
d2	0.26	0.0042	4.531×10^{-3}	1.88	0.725
d2	0.38	0.0038	5.867×10^{-3}	1.88	0.725
d2	0.59	0.0154	1.806×10^{-3}	3.76	0.725
d2	0.59	0.0166	1.821×10^{-3}	3.76	0.725
d2	0.77	0.0504	1.017×10^{-3}	5.63	0.725
d2	0.76	0.0592	8.24×10^{-4}	5.63	0.725
d2	0.82	0.1034	4.89×10^{-4}	7.51	0.725
d2	0.83	0.1159	4.48×10^{-4}	7.51	0.725
d2	0.9	1.0199	2.08×10^{-5}	15.02	0.725
d2	0.92	1.0162	1.88×10^{-5}	15.02	0.725
d3	0.47	0.0245	9.12×10^{-3}	3.76	2
d3	0.45	0.0260	7.90×10^{-3}	3.76	2
d3	0.80	0.0833	5.02×10^{-3}	7.51	2
d3	0.74	0.1278	3.42×10^{-3}	7.51	2
d3	0.80	0.1331	5.42×10^{-3}	15.02	2
d3	0.81	0.2117	3.73×10^{-3}	15.02	2
d4	0.3	0.0028	3.686×10^{-1}	1.88	15
d4	0.29	0.0044	2.5569×10^{-1}	1.88	15
d4	0.43	0.0105	9.7743×10^{-2}	3.76	15
d4	0.5	0.016	9.2701×10^{-2}	3.76	15
d4	0.61	0.0218	6.7168×10^{-2}	5.63	15
d4	0.61	0.0235	5.9689×10^{-2}	5.63	15
d4	0.67	0.0488	2.9586×10^{-2}	7.51	15
d4	0.68	0.0543	2.7332×10^{-2}	7.51	15
d4	0.72	0.1015	9.565×10^{-3}	15.02	15
d4	0.74	0.1327	8.864×10^{-3}	15.02	15

In Figure 4g,h we observe the spectra of ground samples after mixing two different grain sizes. We observe that in most of the cases, the spectra fail to resolve the peak associated with the two different length scales (i.e., grain sizes), but rather, the response is a single peak with a critical frequency approximately given by the mean of the critical frequency for the two independent grain sizes. Figure 4g,h also shows that the characteristic frequency can resolve for two distinctive peaks only in mixtures with drastic differences (>100%) in the grain sizes (e.g., 0.45 mm and 10 mm). Moreover, we can see an increase in-phase (>100%) and quadrature conductivity (>100%) values when increasing the content of the ground material, for instance, in the mixture of grain sizes d2 and d4.

Figure 4i,j presents the spectra measured on the commercial graphite powder with the increasing saline pore fluids. Due to the small grain size, the frequency peak occurs at high frequencies (~200 Hz) at low salinity (0.023 mg/L) and shifts to higher frequencies as the salinity increases (~5000 Hz for 1.15 mg/L), which is consistent with the observations reported by Wu and Peruzzo [15]. The frequency peak and the in-phase and quadrature conductivity values increase with fluid salinity. Similar to Wu and Peruzzo [15], we found that increasing salinity shifts the characteristic frequency to higher frequencies (Table 5) and similar to their 150 μm graphite data set, we found a decrease in the magnitude of the phase response (Figure 4i,j).

Table 5. Cole-Cole parameters of the commercial graphite sample in terms of chargeability (M), normalized chargeability, relaxation time, and the Sodium-chloride (NaCl) content of the pore fluid of the mixture. The volumetric graphite content of the sand-graphite mixture is 2.01%.

d	M	M_n (S/m)	T (s)	NaCl Content (g/L)	σ_f (S/m)
commercial	0.688	0.001	0.00993	0.023	0.005
commercial	0.642	0.002	0.00227	0.046	0.011
commercial	0.651	0.002	0.00240	0.069	0.015
commercial	0.617	0.003	0.00119	0.092	0.020
commercial	0.595	0.003	0.00102	0.092	0.020
commercial	0.584	0.006	0.00045	0.23	0.049
commercial	0.582	0.006	0.00045	0.23	0.050
commercial	0.541	0.010	0.00022	0.46	0.096
commercial	0.553	0.010	0.00022	0.46	0.099
commercial	0.516	0.014	0.00012	0.69	0.144
commercial	0.517	0.014	0.00014	0.69	0.144
commercial	0.508	0.017	0.00011	0.92	0.189
commercial	0.509	0.017	0.00010	0.92	0.192
commercial	0.499	0.021	0.00008	1.15	0.229
commercial	0.507	0.021	0.00008	1.15	0.230
d1	0.435	0.000	0.00851	0	0.003
d1	0.450	0.001	0.00286	0	0.010
d1	0.423	0.005	0.00035	0.092	0.021
d1	0.413	0.006	0.00033	0.23	0.046
d1	0.405	0.008	0.00023	0.23	0.046
d1	0.404	0.009	0.00023	0.46	0.086
d1	0.378	0.015	0.00014	0.46	0.087
d1	0.379	0.015	0.00014	0.92	0.167
d3	0.303	0.001	0.52567	0	0.008
d3	0.300	0.002	0.25820	0.092	0.022
d3	0.298	0.002	0.22127	0.092	0.023
d3	0.283	0.003	0.12993	0.23	0.048
d3	0.270	0.003	0.11120	0.23	0.053
d3	0.278	0.005	0.06865	0.46	0.085
d3	0.279	0.006	0.06461	0.46	0.085
d3	0.282	0.011	0.03538	0.92	0.167
d3	0.283	0.011	0.03316	0.092	0.172

3.3. Interpretation of SIP Signatures

To investigate the correlation between textural information (the grain size of the ground materials) and the electrical properties, we present in Figure 5 the principal component analysis (PCA) computed for each spectra measured in samples with well-defined grain size. In particular, we use the PCA to investigate the correlation between the grain size and the Cole-Cole parameters fitted to each measured spectra (see Tables 3–5). The PCA helps us compare more variables through the fitting to each other orthogonal lines on the set of observations [51]. We can determine the various accounts with the eigenvalues of the principal components. The first two principal components give the axes of the coordinate

system (Figure 5), which describe 88% (in the case of the graphite plugs), 83% (in the case of the disseminated graphite), and 99% (in the case of the commercial graphite samples) of the variation. Every parameter or component has a value between -1 and 1 . These values produce the coefficient matrix, giving the coordinates of the coefficients (see Figure 5). The longer the vector resolved within each component, the higher the influence of the parameter. In the case of the plug measurements, the PCA reveals that the sample volume correlates more to the chargeability than the normalized chargeability, and both contribute to the first principal component (Figure 5a). Figure 5b reveals that while the chargeability and maximum phase values contribute to the first principal component, the grain size, which correlates with the relaxation time the most, contributes the most to the second principal component. The graphite volume correlates more to the normalized chargeability than to the chargeability. Furthermore, in the case of measurements in synthetic graphite powder, the normalized chargeability correlates to the salt content (Figure 5c). The PCA reveals that the chargeability contributes to the first principal component, while the relaxation time contributes to the second principal component; simultaneously, the graphite volume (Figure 5a,b) contributes to both main principal components. Hence, it is clear that the volumetric content of graphite is the main parameter controlling SIP signatures.

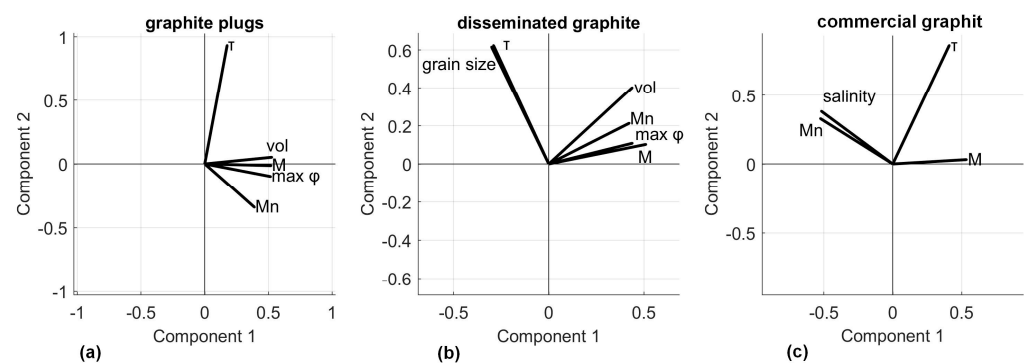


Figure 5. Principal component analysis of the Cole-Cole parameters, in terms of relaxation time (T), volume (vol), chargeability (M), normalized chargeability (M_n), maximum phase value ($\max \varphi$), grain size, and salinity of the (a) graphite plugs, (b) disseminated sediments and (c) commercial graphite.

To establish an experimental model that links our electrical parameters with graphite content and grain size, we present in Figure 6 plots of the chargeability and normalized chargeability against the graphite content, and the relaxation time against the grain size. In Figure 6a, the chargeability (M) and the volumetric graphite content reveal a positive linear relationship in cases with graphite content below 10%. Figure 6a reveals that most of our laboratory measurements can be described with a power-law relationship between chargeability and the graphite content, including samples with 15% graphite. Such a model can be written as

$$\varnothing = a + bM^c \quad (4)$$

where \varnothing represents the graphite volumetric content, and a , b , and c fitting constants.

Equation (4) was observed for different grain sizes; however, we observed different b and c parameters for the small grain sizes (d_1 and d_2) in comparison to those needed for larger grain sizes (d_3 and d_4 , dashed line in Figure 6a). Alternatively, in Figure 6b, we show the correlation between the normalized chargeability (M_n) and graphite volumetric content, which also needs to be adjusted for large grain sizes. Such a power-law relationship can be written as follows:

$$\varnothing = eM_n^f \quad (5)$$

where e and f represent fitting coefficients. As observed in Table 6, the use of Equation (5) results in a coefficient of correlation (R^2) higher than the one observed in Equation (4), likely because involving the normalized chargeability also permits to account for variations in the pore-fluid electrical conductivity (Equation (3)). Lesmes and Frye proposed the

normalized chargeability as the parameter quantifying the polarization magnitude in SIP measurements [52]. They argue that normalizing the chargeability by the electrical conductivity, helps to reduce inferences in the data due to the fluid conductivity. However, plots in Figure 4i,j and Figure 5c shows a dependency between our samples and the fluid conductivity thus, the normalized chargeability offers a more robust approach for the prediction of graphite content from SIP measurements as M_n accounts for the changes in fluid conductivity. This apparent inconsistency is due to the presence of the electrical conductors which is not considered in the study by Lesmes and Frye [52]. The studies by Bückner et al. also revealed a change in the SIP response accompanying variations in the fluid conductivity from a numerical point of view, while Wu and Peruzzo also observed such variations in SIP measurements by changing fluid conductivity in laboratory measurements [15,28].

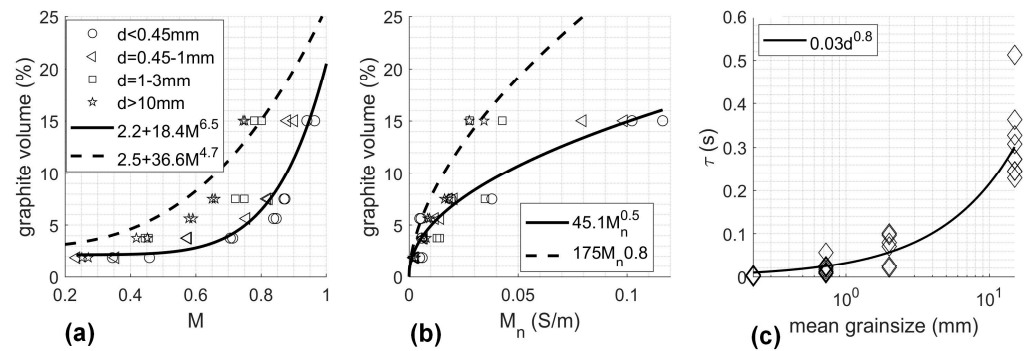


Figure 6. Cole-Cole parameters versus volumetric graphite content. (a) Chargeability M versus the volumetric graphite content of the sand-graphite sediment samples. (b) Normalized chargeability, M_n versus the volumetric graphite content. (c) Mean grain size versus the characteristic relaxation time τ of the sand-graphite sediment samples (all samples with the grain ID d1 to d4). The dashed and solid lines show the fitted power-law relationships.

Table 6. Cole-Cole parameter of the collected sediments in terms of chargeability (M), normalized chargeability (M_n) and relaxation time (τ), the volumetric graphite content in the sand-graphite mixture and the mean grain size of the graphite sediments.

Fitted Parameters	Grain ID	Fitted Equation	Quality of Fit
Graphite content and M	d1 and d2	$\varnothing = 2.2 + 18.4 \cdot M^{6.5}$	$R^2 = 0.84$
	d3 and d4	$\varnothing = 2.5 + 36.6 \cdot M^{4.7}$	$R^2 = 0.85$
Graphite content and M_n	d1 and d2	$\varnothing = 45.1 \cdot M_n^{0.5}$	$R^2 = 0.94$
	d3 and d4	$\varnothing = 175 \cdot M_n^{0.8}$	$R^2 = 0.76$
Grain size and τ	all	$\tau = 0.03 \cdot d^{0.8}$	$R^2 = 0.88$
Graphite content and M	Plugs and d4	$\varnothing = 25 \cdot M^{1.8}$	$R^2 = 0.72$
Graphite content and M_n	Plugs and d4	$\varnothing = 108.7 \cdot M_n^{0.5}$	$R^2 = 0.55$
Salinity and M	commercial	$M = 0.4\sigma_{fl}^{-0.08}$	$R^2 = 0.97$
	d1	$M = 0.4\sigma_{fl}^{-0.03}$	$R^2 = 0.75$
	d3	$M = 0.3\sigma_{fl}^{-0.03}$	$R^2 = 0.50$
Salinity and M_n	commercial	$M_n = 0.001 + \sigma_{fl} \cdot 0.09$	$R^2 = 0.99$
	d1	$M_n = 0.002 + \sigma_{fl} \cdot 0.09$	$R^2 = 0.82$
	d3	$M_n = 0.0003 + \sigma_{fl} \cdot 0.06$	$R^2 = 0.99$
Salinity and τ	commercial	$\tau = 0.002\sigma_{fl}^{-1.65}$	$R^2 = 0.99$
	d1	$\tau = 0.015\sigma_{fl}^{-1.09}$	$R^2 = 0.99$
	d3	$\tau = 10.82\sigma_{fl}^{-0.8}$	$R^2 = 0.99$

Consistent with previous studies [25], we also observed an increase in relaxation time with increasing grain size (Figure 6c). In the case of our measurements, we obtained a power-law relationship, written as:

$$\tau = 0.03 \cdot d^{0.8} \tag{6}$$

As observed in Figure 6c, the Equation (6) fits our data (correlation coefficient of $R^2 = 0.88$), as in general, we observe a large variability in the relaxation time for the different grain sizes. This may also reflect a larger heterogeneity in the actual grain size of the particles in d4.

We present the exact Cole-Cole parameters in terms of chargeability, normalized chargeability and relaxation time and the graphite volume for each grain size in Table 4. In contrast, Table 6 shows the fitted parameters for the models describing the link between Cole-Cole parameters and the graphite content and grain size (i.e., associated with Equations (4) and (5)). Similar to Pelton et al. [20], we found that the chargeability increases—and the relaxation time decreases—with increasing graphite content, whereas the chargeability decreases—and the relaxation time increases—with increasing the grain size.

Although we have resolved a relationship between graphite content and the SIP response for laboratory measurements, evaluating the observed relationship for field measurements is still necessary. To this end, we present in Figure 7 spectra extracted from the complex conductivity imaging results of the profile P2b at a distance of 50 m and 125 m close to the surface ($z > 450$ m). Moreover, in Figure 7 we present the spectra measured on the site with the PSIP unit (at positions Z1 and Z5, referred to as in-situ PSIP from now on). For the sake of comparison, we present in Figure 7 also the spectra in ground samples with the largest grain size (d4). Figure 7 reveals similar spectra for those extracted from the imaging plane (at a profile distance of 125m), those collected in-situ PSIP, and in the ground samples. The in-situ PSIP and imaging measurements (carried out with the DAS1 instrument) were conducted on different days, which can explain some spectral differences. The field spectra (both DAS1 and PSIP measurements) do not reveal a clear frequency peak, i.e., the spectra are almost flat, clearly different from the measurements in samples with well-defined grain size samples. Hence, our measurements suggest that materials in Zettlitz quarry are well sorted (i.e., even distribution of different grain sizes), at least within the range of frequencies captured with our measurements. Nonetheless, Figure 7 indicates a slight increase with increasing frequency, suggesting that the frequency peak may be found at frequencies above 100 Hz, which, according to the mechanistic models, is indicative of the dominating fine grains, as predicted by the mechanistic models [25,27,28]. However, field data measured at higher frequencies is needed to thoroughly investigate the possible frequency peak.

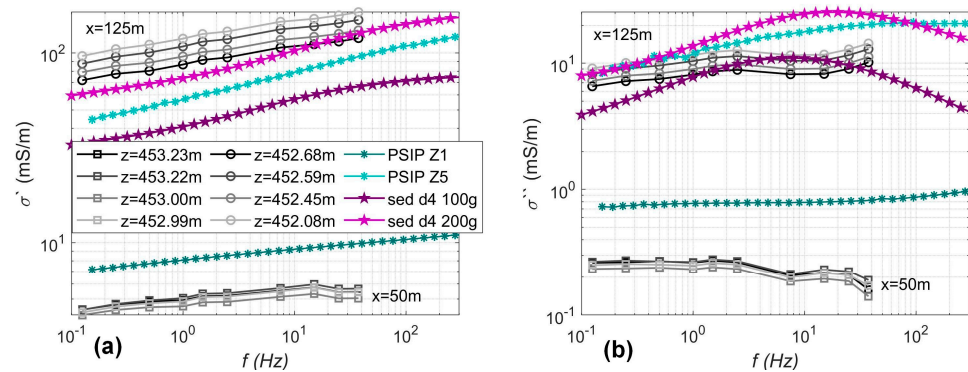


Figure 7. Complex conductivity spectra in terms of (a) in-phase and (b) quadrature conductivity, exported from the imaging results of Profile P2b (circle and square), the in situ PSIP measurements (Z1, Z5—star) and the laboratory measurements of the collected sediments (d4—pentagon). The z coordinate represents the height of the imaging results, and the x coordinates the position at the profile length.

In Figure 8, we present plots of the graphite volumetric content as a function of chargeability and normalized chargeability. Here we present only the parameters obtained for spectra measured in plugs 2 and 4 as well as those obtained for the ground samples with the largest grain (d4). SIP data for plugs 2 to 4 indicate that these correspond to similar composition, although the exact graphite content is only known for plug 4. We account for the size of the samples (plugs and ground material) to compute the graphite volumetric content. We found a power-law correlation between the chargeability and graphite volume (Figure 8a) and normalized chargeability and graphite volume (Figure 8b) and applied the Equations (7) and (8) (respectively) to determine the graphite content of both the rock and the ground samples. The obtained models revealed a better coefficient of correlation ($R^2 = 0.72$) for Equation (7) than for Equation (8), as observed in Table 6, and can be written as:

$$\varnothing = 25 \cdot M^{1.8} \quad (7)$$

$$\varnothing = 108.7 \cdot M_n^{0.5} \quad (8)$$

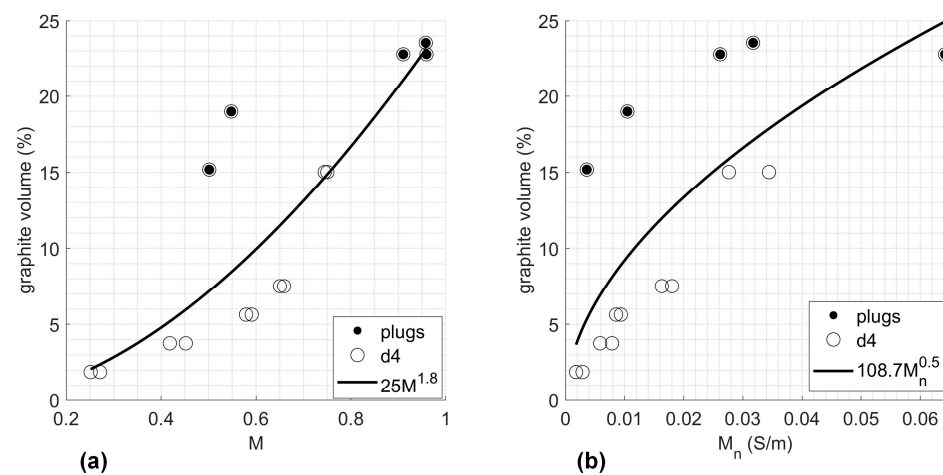


Figure 8. Cole-Cole parameters in terms of (a) chargeability and (b) normalized chargeability versus the volume percentage covered by a plug within the measurement cell.

Assuming that the plots presented in Figure 8 represent an experimental model linking the electrical properties (i.e., M and M_n) and the graphite content for heterogeneous samples, we believe that Equations (7) and (8) may be applicable for all SIP measurements collected at the Zettlitz site. In this regard, we assume that the plugs provide a representative sample for the real materials, yet we require the data collected in ground samples, where the graphite content was measured through X-ray fluorescence spectroscopy and LECO analysis. Such methods for direct quantification of graphite content are not possible on larger samples (i.e., the plugs) or in-situ.

3.4. The Dependency of SIP Parameters on Pore Fluid Conductivity

Wu and Peruzzo reported a strong relationship between pore fluid salinity and chargeability [15]. In particular, they specified that increasing salinity and decreasing chargeability correlate with the 150 μm grain size graphite if the sample contains 5% graphite. However, Revil et al. found the chargeability to be independent for measurements varying the pore fluid in a conductivity range between 0.1 and 10 S/m [33]. To better evaluate the pore fluid dependency of our SIP signatures (and the derived petrophysical model), we conducted SIP measurements in the lab, varying the pore fluid conductivity at different intervals between 0.03 and 0.23 mS/m on ground samples as well as commercial graphite with well-defined grain size.

Figure 9a shows that the chargeability (M) of commercial graphite samples and site-specific rock samples (volumetric content is 2.01% in all samples; values are presented in

Table 5) decreases exponentially when increasing the pore fluid conductivity (σ_f) in a range from 0.005 S/m to 0.25 S/m. Here we observe the highest chargeability values ($M = 0.7$) for commercial graphite samples (grain size < 0.07 mm), which is more than two times higher than the value observed for the ground samples d3 ($M = 0.3$ for). Figure 9b shows a clear linear relationship between the normalized chargeability (M_n) and σ_f . Additionally, we observe in Figure 9c that the relaxation time (τ) decreases exponentially when increasing σ_f from 0.005 S/m to 0.25 S/m.

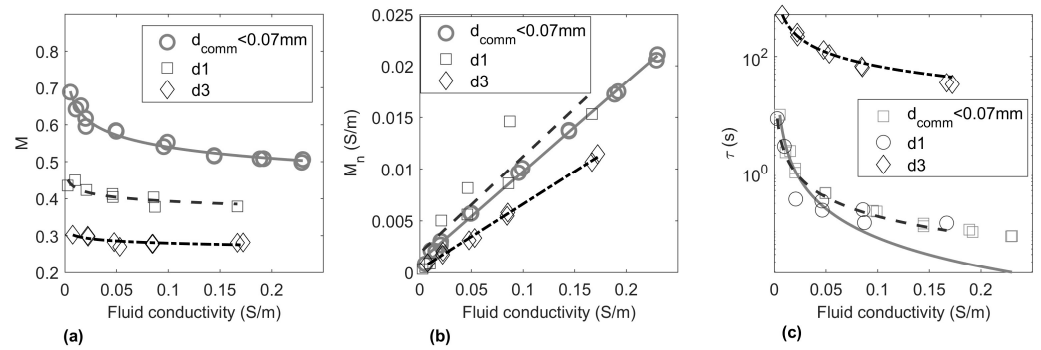


Figure 9. Results from the measurements in the commercial graphite sample as well as in the particles from the rock sample by varying NaCl content of the pore fluid versus the Cole-Cole parameters in terms of (a) chargeability, (b) normalized chargeability and (c) relaxation time.

Similar to Wu and Peruzzo and Gurin et al., our results demonstrate the dependency on fluid conductivity of SIP signatures in graphite measurements [13,15]. For our experiments, we applied a solution in the conductivity range between 0.005 and 0.25 S/m, corresponding to the pore fluid conductivity we measured at sites with no visible graphite on the surface and graphite outcrop. Furthermore, we conducted measurements with increasing pore fluid salinity on samples collected on the field and found the same behavior: a decrease in chargeability with increasing salinity as well as an increase in the normalized chargeability with increasing the fluid conductivity (Table 5). However, in the case of the grain size d3 and fluid conductivity above 0.08 S/m, the chargeability remains constant. Bucker et al. found that in the case of big particles ($d > 60 \mu\text{m}$), where the volume diffusion dominates, the relaxation time has negligible sensitivity to the changes in the pore fluid conductivity [28]. However, it is sensitive to the reaction current. We observe a decrease in relaxation time with increasing fluid conductivity. The decrease is larger at low salinity (< 0.05 S/m) with almost constant relaxation time values at high salinity (> 0.05 S/m).

3.5. Field-Scale Quantification of Graphite Content

Built on Equations (7) and (8) derived from SIP measurements with our laboratory samples, we could estimate the graphite content using the SIP profiles under investigation using the fitted Equations (7) and (8) (see also Table 6). In Figure 10, we present the relative RMS error (rRMSE) of the Cole-Cole fit for each pixel. The rRMSE values are mostly below 20%, which is considered a reasonably good model fit [53]. In the case of profile P1 (Figure 10a–c), M and M_n resolve for a similar low graphite content ($< 10\%$). The graphite content is slightly higher ($\sim 13\%$) within the first 100 m along the profile direction, in a layer extending to the surface and ca. 10 m depth. In the case of P7, Figure 10d,e show a significant difference in the estimated graphite content for estimations using M and M_n . For the former, the highest graphite content ($\sim 20\%$) is resolved in the second half of the profile (> 75 m along profile distance), whereas the highest graphite content (up to 40%) is observed in the first half of the profile if we use the model based on M_n . Significant discrepancies are also observed for P2 and P2b (Figure 10). The estimations based on Equation (8) using M_n (obtained from the biggest grain size, d4 and the plugs due to their most probable similarities to the field properties) agrees exactly with the expected graphite-rich area, as obtained from geological (i.e., surface) observations. Hence, these

results demonstrate that Equation (8) is best suited to estimate the graphite content at sites where the graphite content is significantly larger than 20%.

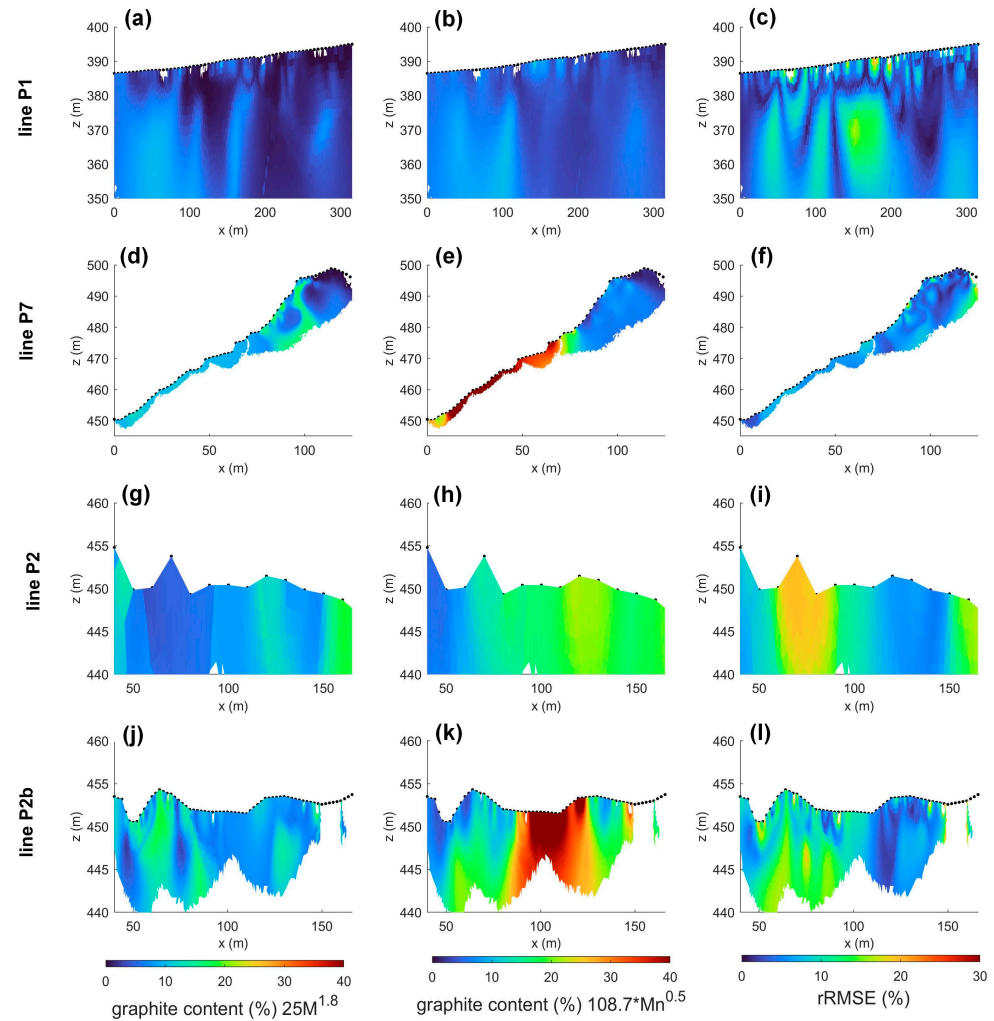


Figure 10. The calculated volumetric content of graphite (using Equations (6) and (7)) based on the chargeability (a,d,g,j), the normalized chargeability (b,e,h,k) and the relative RMS error of the Cole-Cole fit (c,f,i,l) along profiles P1, P7 and P2.

Abdulsamad et al. concluded that the graphite content could be estimated with their linear model in the case of low graphite content, while in the case of high graphite content, high conductivity is observable [16]. Our results suggest that chargeability can be used to estimate graphite content in the case of low graphite content. Although Mao et al. suggest that the normalized chargeability is meaningless in the case of ore bodies, our results suggest that we can estimate graphite content with the normalized chargeability [54]. Further work is required to include the relaxation time in the empirical model to achieve a more accurate graphite content estimation.

4. Conclusions

We studied graphite samples to obtain the Cole-Cole parameters and estimate the graphite content in different SIP imaging fields. We observed frequency dependence of the SIP imaging and laboratory SIP measurements conducted on the collected and commercial graphite samples. These samples included both disseminated unconsolidated materials and plugs drilled from graphitic rock formations. We found a power-law correlation between the normalized chargeability and volumetric graphite content as well as between the chargeability and volumetric graphite content of the disseminated graphite samples

and the drilled plugs. While the chargeability shows high values for the smaller grain size, the normalized chargeability tends to be more sensitive to the grain size differences at high graphite concentrations (>10%). The graphite content obtained with the normalized chargeability is consistent with field observations. Furthermore, we investigated the pore fluid salinity dependence of graphite sediments with different grain sizes. Our results suggest that the pore fluid salinity influences the Cole-Cole chargeability, normalized chargeability and relaxation time, especially at low pore fluid salinity changes. Our results open the possibility of applying normalized chargeability for improved graphite content characterization and estimation. Moreover, we emphasize the importance of employing stochastic approaches for geophysical data inversion to ascertain uncertainty in electrical property assessments. This aspect is pivotal for accurately gauging the uncertainty in our graphite estimations and should form the cornerstone of forthcoming research endeavors in this field.

Author Contributions: The conceptualization of this project was led by A.F.-O., with the contribution of T.K., A.F.-O. and T.K. designed the experimental setup, T.K. and L.A. performed fieldwork preparation, data collection, and analysis. C.B. performed the chemical composition analysis. T.K. wrote the first draft of the manuscript and all authors commented on subsequent versions. A.F.-O. provided supervision for T.K. throughout the whole research project. Project administration and funding acquisition: A.F.-O. All authors have read and agreed to the published version of the manuscript.

Funding: Open Access Funding by TU Wien.

Data Availability Statement: Data are available upon request to A.F.-O.

Acknowledgments: We acknowledge TU Wien Bibliothek for financial support through its Open Access Funding Program. The research was partially funded as part of the implementation of the Deposits Act (Vollzug des Lagerstättengesetzes-VLG) on behalf of the Federal Ministry of Science, Research and Economy and the Federal Ministry of Finance.

Conflicts of Interest: The authors declare no conflicts of interest.

References

1. Wang, Z.-R.; Li, B.; Liu, H.-B.; Zhang, Y.-X.; Qin, X. Degradation characteristics of graphite tailings cement mortar subjected to freeze-thaw cycles. *Constr. Build. Mater.* **2020**, *234*, 117422. [[CrossRef](#)]
2. Jara, A.D.; Betemariam, A.; Woldetinsae, G.; Kim, J.Y. Purification, application and current market trend of natural graphite: A review. *Int. J. Min. Sci. Technol.* **2019**, *29*, 671–689. [[CrossRef](#)]
3. Rui, X.; Geng, Y.; Zhuang, M.; Xiao, S.; Sun, X. Emergency-based environmental accounting of graphite anode material production. *J. Clean. Prod.* **2022**, *339*, 130705. [[CrossRef](#)]
4. Vozoff, K. Electromagnetic methods in applied geophysics. *Geophys. Surv.* **1980**, *4*, 9–29. [[CrossRef](#)]
5. Aigner, L.; Werthmüller, D.; Orozco, A.F. Sensitivity analysis of inverted model parameters from transient electromagnetic measurements affected by induced polarization effects. *J. Appl. Geophys.* **2024**, *223*, 105334. [[CrossRef](#)]
6. Shao, Z.; Revil, A.; Mao, D.; Wang, D. Induced polarization signature of coal seam fires. *Geophys. J. Int.* **2017**, *208*, 1313–1331. [[CrossRef](#)]
7. Katona, T.; Gilfedder, B.S.; Frei, S.; Bücken, M.; Flores-Orozco, A. High-resolution induced polarization imaging of biogeochemical carbon turnover hotspots in a peatland. *Biogeosciences* **2021**, *18*, 4039–4058. [[CrossRef](#)]
8. Flores-Orozco, A.; Gallistl, J.; Steiner, M.; Brandstätter, C.; Fellner, J. Mapping biogeochemically active zones in landfills with induced polarization imaging: The Heferlbach landfill. *Waste Manag.* **2020**, *107*, 121–132. [[CrossRef](#)]
9. Schlumberger, C. *Study of Underground Electrical Prospecting*; University of California Libraries: Merced, CA, USA, 1920.
10. Seigel, H.; Nabighian, M.; Parasnis, D.S.; Vozoff, K. The early history of the induced polarization method. *Lead. Edge* **2007**, *26*, 312–321. [[CrossRef](#)]
11. Kinchin, G. The electrical properties of graphite. *Proc. R. Soc. Lond. Ser. A Math. Phys. Sci.* **1953**, *217*, 9–26. [[CrossRef](#)]
12. Klein, J.; Shuey, R. Nonlinear impedance of mineral-electrolyte interfaces: Part II. Galena, chalcopyrite, and graphite. *Geophysics* **1978**, *43*, 1235–1249. [[CrossRef](#)]
13. Gurin, G.; Titov, K.; Ilyin, Y.; Tarasov, A. Induced polarization of disseminated electronically conductive minerals: A semi-empirical model. *Geophys. J. Int.* **2015**, *200*, 1555–1565. [[CrossRef](#)]
14. Revil, A.; Coperey, A.; Shao, Z.; Florsch, N.; Fabricius, I.L.; Deng, Y.; Delsman, J.; Pauw, P.; Karaoulis, M.; De Louw, P. Complex conductivity of soils. *Water Resour. Res.* **2017**, *53*, 7121–7147. [[CrossRef](#)]
15. Wu, Y.; Peruzzo, L. Effects of salinity and pH on the spectral induced polarization signals of graphite particles. *Geophys. J. Int.* **2020**, *221*, 1532–1541. [[CrossRef](#)]

16. Abdulsamad, F.; Revil, A.; Ahmed, A.S.; Coperey, A.; Karaoulis, M.; Nicaise, S.; Peyras, L. Induced polarization tomography applied to the detection and the monitoring of leaks in embankments. *Eng. Geol.* **2019**, *254*, 89–101. [[CrossRef](#)]
17. Börner, J.H.; Girault, F.; Bhattarai, M.; Adhikari, L.B.; Deldicque, D.; Perrier, F.; Spitzer, K. Anomalous complex electrical conductivity of a graphitic black schist from the Himalayas of central Nepal. *Geophys. Res. Lett.* **2018**, *45*, 3984–3993. [[CrossRef](#)]
18. Zimmermann, E.; Kemna, A.; Berwix, J.; Glaas, W.; Vereecken, H. EIT measurement system with high phase accuracy for the imaging of spectral induced polarization properties of soils and sediments. *Meas. Sci. Technol.* **2008**, *19*, 094010. [[CrossRef](#)]
19. Zimmermann, E.; Huisman, J.; Mester, A.; Van Waasen, S. Correction of phase errors due to leakage currents in wideband EIT field measurements on soil and sediments. *Meas. Sci. Technol.* **2019**, *30*, 084002. [[CrossRef](#)]
20. Pelton, W.H.; Ward, S.H.; Hallof, P.; Sill, W.; Nelson, P.H. Mineral discrimination and removal of inductive coupling with multifrequency IP. *Geophysics* **1978**, *43*, 588–609. [[CrossRef](#)]
21. Wait, J.R.; Gruszka, T.P. On electromagnetic coupling “removal” from induced polarization surveys. *Geoexploration* **1986**, *24*, 21–27. [[CrossRef](#)]
22. Binley, A.; Kemna, A. DC resistivity and induced polarization methods. In *Hydrogeophysics*; Springer: Dordrecht, The Netherlands, 2005; pp. 129–156.
23. Kemna, A.; Binley, A.; Cassiani, G.; Niederleithinger, E.; Revil, A.; Slater, L.; Williams, K.H.; Orozco, A.F.; Haegel, F.; Hördt, A. An overview of the spectral induced polarization method for near-surface applications. *Near Surf. Geophys.* **2012**, *10*, 453–468. [[CrossRef](#)]
24. Orozco, A.F.; Aigner, L.; Gallistl, J. Investigation of cable effects in spectral induced polarization imaging at the field scale using multicore and coaxial cables. *Geophysics* **2021**, *86*, E59–E75. [[CrossRef](#)]
25. Wong, J. An electrochemical model of the induced-polarization phenomenon in disseminated sulfide ores. *Geophysics* **1979**, *44*, 1245–1265. [[CrossRef](#)]
26. Revil, A.; Florsch, N.; Mao, D. Induced polarization response of porous media with metallic particles—Part 1: A theory for disseminated semiconductors. *Geophysics* **2015**, *80*, D525–D538. [[CrossRef](#)]
27. Bucker, M.; Orozco, A.F.; Kemna, A. Electrochemical polarization around metallic particles—Part 1: The role of diffuse-layer and volume-diffusion relaxation. *Geophysics* **2018**, *83*, E203–E217. [[CrossRef](#)]
28. Bucker, M.; Undorf, S.; Flores Orozco, A.; Kemna, A. Electrochemical polarization around metallic particles—Part 2: The role of diffuse surface charge. *Geophysics* **2019**, *84*, E57–E73. [[CrossRef](#)]
29. Slater, L.; Ntarlagiannis, D.; Wishart, D. On the relationship between induced polarization and surface area in metal-sand and clay-sand mixtures. *Geophysics* **2006**, *71*, A1–A5. [[CrossRef](#)]
30. Revil, A.; Abdel Aal, G.Z.; Atekwana, E.A.; Mao, D.; Florsch, N. Induced polarization response of porous media with metallic particles—Part 2: Comparison with a broad database of experimental data. *Geophysics* **2015**, *80*, D539–D552. [[CrossRef](#)]
31. Revil, A.; Sleevi, M.F.; Mao, D. Induced polarization response of porous media with metallic particles—Part 5: Influence of the background polarization. *Geophysics* **2017**, *82*, E77–E96. [[CrossRef](#)]
32. Revil, A.; Mao, D.; Shao, Z.; Sleevi, M.F.; Wang, D. Induced polarization response of porous media with metallic particles—Part 6: The case of metals and semimetals. *Geophysics* **2017**, *82*, E97–E110. [[CrossRef](#)]
33. Revil, A.; Coperey, A.; Mao, D.; Abdulsamad, F.; Ghorbani, A.; Rossi, M.; Gasquet, D. Induced polarization response of porous media with metallic particles—Part 8: Influence of temperature and salinity. *Geophysics* **2018**, *83*, E435–E456. [[CrossRef](#)]
34. Weber, L. *Die Geologischen Grundlagen des Grafitbergbaues in Niederösterreich*; Geologisches Bundesanstalt: Vienna, Austria, 1987.
35. Schrauder, M.; Beran, A.; Hoernes, S.; Richter, W. Herkunft und Genese von graphitführenden Gesteinen der Bunten Serie aus der Böhmischen Masse (Österreich). *Mineral. Petrol.* **1993**, *49*, 175–188. [[CrossRef](#)]
36. Orozco, A.F.; Kemna, A.; Zimmermann, E. Data error quantification in spectral induced polarization imaging. *Geophysics* **2012**, *77*, E227–E237. [[CrossRef](#)]
37. Fiandaca, G.; Auken, E.; Christiansen, A.V.; Gazoty, A. Time-domain-induced polarization: Full-decay forward modeling and 1D laterally constrained inversion of Cole-Cole parameters. *Geophysics* **2012**, *77*, E213–E225. [[CrossRef](#)]
38. Fiandaca, G.; Ramm, J.; Binley, A.; Gazoty, A.; Christiansen, A.V.; Auken, E. Resolving spectral information from time domain induced polarization data through 2-D inversion. *Geophys. J. Int.* **2013**, *192*, 631–646. [[CrossRef](#)]
39. Binley, A.; Slater, L. *Resistivity and Induced Polarization: Theory and Applications to the Near-Surface Earth*; Cambridge University Press: Cambridge, UK, 2020; ISBN 1-108-69459-4.
40. Sumner, J.S. *Principles of Induced Polarization for Geophysical Exploration*; Elsevier: Amsterdam, The Netherlands, 2012; ISBN 0-444-59987-8.
41. Ward, S.H. *The Resistivity and Induced Polarization Methods*; European Association of Geoscientists & Engineers: Utrecht, the Netherlands, 1988; p. cp-214.
42. Rücker, C.; Günther, T.; Wagner, F.M. pyGIMLi: An open-source library for modelling and inversion in geophysics. *Comput. Geosci.* **2017**, *109*, 106–123. [[CrossRef](#)]
43. Dahlin, T.; Zhou, B. Multiple-gradient array measurements for multichannel 2D resistivity imaging. *Near Surf. Geophys.* **2006**, *4*, 113–123. [[CrossRef](#)]
44. Orozco, A.F.; Williams, K.H.; Kemna, A. Time-lapse spectral induced polarization imaging of stimulated uranium bioremediation. *Near Surf. Geophys.* **2013**, *11*, 531–544. [[CrossRef](#)]

45. Kemna, A. *Tomographic Inversion of Complex Resistivity: Theory and Application*; Der Andere Verlag: Berlin, Germany, 2000; ISBN 3-934366-92-9.
46. Bairlein, K.; Hördt, A.; Nordsiek, S. The influence on sample preparation on spectral induced polarization of unconsolidated sediments. *Near Surf. Geophys.* **2014**, *12*, 667–678. [[CrossRef](#)]
47. Inamdar, S.N.; Bhat, M.A.; Haram, S.K. Construction of Ag/AgCl reference electrode from used felt-tipped pen barrel for undergraduate laboratory. *J. Chem. Educ.* **2009**, *86*, 355. [[CrossRef](#)]
48. Revil, A.; Florsch, N. Determination of permeability from spectral induced polarization in granular media. *Geophys. J. Int.* **2010**, *181*, 1480–1498. [[CrossRef](#)]
49. Li, Z.; Liu, D.; Cai, Y.; Ranjith, P.; Yao, Y. Multi-scale quantitative characterization of 3-D pore-fracture networks in bituminous and anthracite coals using FIB-SEM tomography and X-ray μ -CT. *Fuel* **2017**, *209*, 43–53. [[CrossRef](#)]
50. Hupfer, S.; Martin, T.; Weller, A.; Günther, T.; Kuhn, K.; Nginjio, V.D.N.; Noell, U. Polarization effects of unconsolidated sulphide-sand-mixtures. *J. Appl. Geophys.* **2016**, *135*, 456–465. [[CrossRef](#)]
51. Wold, S.; Esbensen, K.; Geladi, P. Principal component analysis. *Chemom. Intell. Lab. Syst.* **1987**, *2*, 37–52. [[CrossRef](#)]
52. Lesmes, D.P.; Frye, K.M. Influence of pore fluid chemistry on the complex conductivity and induced polarization responses of Berea sandstone. *J. Geophys. Res. Solid Earth* **2001**, *106*, 4079–4090. [[CrossRef](#)]
53. Despotovic, M.; Nedic, V.; Despotovic, D.; Cvetanovic, S. Evaluation of empirical models for predicting monthly mean horizontal diffuse solar radiation. *Renew. Sustain. Energy Rev.* **2016**, *56*, 246–260. [[CrossRef](#)]
54. Mao, D.; Revil, A.; Hinton, J. Induced polarization response of porous media with metallic particles—Part 4: Detection of metallic and nonmetallic targets in time-domain-induced polarization tomography. *Geophysics* **2016**, *81*, D359–D375. [[CrossRef](#)]

Disclaimer/Publisher’s Note: The statements, opinions and data contained in all publications are solely those of the individual author(s) and contributor(s) and not of MDPI and/or the editor(s). MDPI and/or the editor(s) disclaim responsibility for any injury to people or property resulting from any ideas, methods, instructions or products referred to in the content.